Noise-driven wave transitions on a vertically falling film

By HSUEH-CHIA CHANG, EVGENY A. DEMEKHIN
AND SERGEY S. SAPRIKIN†

Department of Chemical Engineering, University of Notre Dame, Notre Dame, IN 46556, USA

We decipher the rich and complex two-dimensional wave transition and evolution dynamics on a falling film both theoretically and numerically. Small-amplitude white noise at the inlet is filtered by the classical linear instability into a narrow Gaussian band of primary frequency harmonics centred about ω_m. Weakly nonlinear zero-mode excitation and a secondary modulation instability then introduce a distinct characteristic modulation frequency $\Delta \ll \omega_m$. The primary wave field evolves into trains of solitary pulses with an average wave period of $2\pi/\omega_m$. Abnormally large 'excited' pulses appear within this train at a relative frequency of Δ/ω_m due to the modulation. The excited pulses travel faster than the equilibrium ones and eliminate them via coalescence to coarsen the pulse field downstream. The linear coarsening of wave period downstream is a universal $(0.015/\langle u \rangle)\,\text{s}\,\text{cm}^{-1}$ and the final wave frequency is the modulation frequency Δ for $0.1 < \delta < 0.4$ where $\langle u \rangle$ is the flat-film average Nusselt velocity, $\delta = (3R^2/W)^{1/3}/15$ is a normalized Reynolds number, R is the flat-film Reynolds number and W the Weber number.

1. Introduction

The wave fields of an open-flow, convectively unstable system often exhibit a large range of wave amplitude, wavelength and wave speed downstream. Typically, linear Orr–Sommerfeld hydrodynamic theories can only capture the wave characteristics of small-amplitude waves at inception near the inlet. This deficiency of linear theory is especially acute for convectively unstable systems with a long-wave instability – whose unstable band of wavenumbers extends to zero. Such longwave instabilities can eventually produce pulse-like solitary waves, each pulse containing a large number of phase-locked Fourier harmonics (Chang 1994; Cheng & Chang 1995). Hence, not only do the wave statistics vary greatly, but the wave shape can also change rapidly downstream in such systems. The normal-mode approximation made in Orr–Sommerfeld theories, for one, cannot be applied to the pulse-like localized wave structures. A completely different approach, necessarily involving nonlinear wave theories, must then be utilized to decipher wave dynamics beyond their inception region, which is often limited to within a few cm of the inlet. For a practical open-flow system longer than 10 cm, much of the wave dynamics in the channel is hence beyond linear theory.

A good prototype of a convectively unstable, open-flow system is the falling film. Earlier experiments by Stainthorp & Allen (1965), Krantz & Goren (1971), Chu & Dukler (1974) and Liu & Gollub (1993) have shown that small-amplitude sinusoidal

† Permanent address: Department of Applied Mathematics, Kuban State University, Krasnodar 350072, Russia.

waves at the inlet can evolve rapidly into solitary pulses within 20 cm for a vertical film and longer for an inclined one. The wave speed, wave amplitude and wavelength can then increase downstream by nearly one order of magnitude after the transition to solitary pulses.

Significant effort has been devoted to the construction of the equilibrium pulses and their interaction dynamics (Chang, Demekhin & Kopelevich 1993, 1995a; Chang, Demekhin & Kalaidin 1995b; Salamon, Armstrong & Brown 1994). The pulses have very large amplitudes – as large or larger than the thickness of the substrate they sit on. They have an asymmetric shape with a steep front profile relieved by capillary ripples (see the wave structures near the exit in figure 1). When excess liquid is inserted into a pulse, it drains out gradually with very specific dynamics. Such an 'excited' pulse with extra liquid is larger and faster than the unperturbed equilibrium ones. However, due to the drainage, both its amplitude and speed approach those of an equilibrium pulse asymptotically in time. Moreover, the excess amplitude and the excess speed (with respect to those of the equilibrium pulses) at any given time are found experimentally to be linearly correlated (Alekseenko, Nakoryakov & Pokusaev 1994; Vlachogiannis & Bontozoglou 2001). Chang, Demekhin & Kalaidin (1998) have studied the dynamics of 'excited' pulses by developing a spectral theory for the pulses. The drainage rate of the excess mass, for example, can be captured by resonance poles of the pulse spectrum. Both the excess amplitude and mass decay exponentially in time as governed by the dominant resonance pole. Linear coupling between this resonance pole governing pulse mass/amplitude and the usual translational discrete mode governing pulse position/speed yields the linear correlation between the speed and amplitude of the decaying excited pulse. This correlation, in turn, dictates that both the excess amplitude and speed of a specific excited pulse decay linearly downstream. Some excited pulses are always found in a noise-driven wave field (Chang, Demekhin & Kalaidin 1996a; Chang, Demekhin & Ye 1996b). They travel faster and capture their smaller front neighbours in irreversible coalescence cascades, provided their excess speed does not decay to zero before the coalescence events. The capture adds additional excess mass to the coalesced pulse and sustains both the excited pulse and the cascade. Such excited pulse-driven events give rise to a linear coarsening of the pulse field downstream (Chang *et al.* 1996a, b). The coalescence events dominate the pulse dynamics and they stop when the pulse separation is so large that the excess mass acquired after each coalescence drains out completely before the next pulse can be captured or when all equilibrium pulses have been captured. A key to this coalescence-driven wave coarsening dynamics is the density of the excited pulses, which has remained undetermined. Curiously, this density seems to produce a universal pulse coarsening rate that is insensitive to inlet noise and flow conditions (Chang *et al.* 1996a, b).

It is shown here that this key excited pulse density is determined during the transition from sinusoidal waves to pulses. As such, much of the subsequent wave dynamics, the pulse coarsening rate, the final pulse separation etc., are fully specified during this transition. This observation allows us to construct a general theory that can predict all realistic wave dynamics on a falling film as functions of Reynolds and Weber numbers and the inlet noise amplitude. The role of the noise amplitude is mainly to specify the location of each wave transition. The generic transition sequence and the dynamics within each regime remain insensitive to noise amplitude. Most intriguingly, within a large range of pratically important Reynolds numbers (about 10 to 40 for water) the wave period coarsening rate with respect to downstream distance is indeed a universal constant divided by the average flat-film velocity.

2. Model equations and numerical simulation

We are as yet unable to carry out extensive simulations of the transient Navier–Stokes equation in an extended domain (> 1 m) with persistent broad-banded noise at the inlet. The major obstacle is the viscous dissipation term in the downstream x-direction, which introduces upstream momentum feedback and necessitates extensive iterations over the extended domain. As discussed earlier (Chang 1994), this obstacle can be removed by carrying out a boundary layer long-wave expansion. The key $\partial^2 u / \partial x^2$ term is omitted and the normal momentum balance is simply a balance between hydrostatic and capillary pressures. The boundary layer equations also possesses certain symmetries, like those for the Blasius solution for momentum boundary layers, that allow us to eliminate one parameter from the problem.

For the vertical falling film considered here, a single parameter $\delta = (3R^2/W)^{1/3}/15$ remains, where $R = \langle u \rangle h_N / v$ and $W = \sigma / \rho \langle u \rangle^2 h_N$ are the Reynolds and Weber numbers defined on the Nusselt flat-film thickness $h_N = (3v^2/g)^{1/3} R^{1/3}$ and flat-film average velocity $\langle u \rangle = (g h_N^2 / 3v)$. For water, these parameters can be expressed conveniently as a function of R only: $\delta = R^{11/9}/167.6$, $h_N = 0.0074 R^{1/3}$ cm and $\langle u \rangle = 1.55 R^{2/3}$ cm s^{-1}. A rule of thumb is that R is about 100 times the normalized Reynolds number δ.

The transformation that exploits the symmetries of the boundary layer equation to eliminate one parameter involves the stretching parameter $\kappa = (WR/3)^{1/3}$ (see, for example, Chang *et al.* 1993). For water, this parameter can conveniently be expressed as a function of R only, $\kappa = 11.17 R^{-2/9}$. Using κh_N to scale x, h_N to scale y, $\langle u \rangle$ to scale u, $\langle u \rangle / \kappa$ to scale v and $\kappa h_N / \langle u \rangle$ to scale time, the two-dimensional boundary layer equations for the falling film become

$$\frac{\partial u}{\partial t} + u \frac{\partial u}{\partial x} + v \frac{\partial u}{\partial y} = \frac{1}{5\delta} \left(\frac{\partial^3 h}{\partial x^3} + \frac{1}{3} \frac{\partial^2 u}{\partial y^2} + 1 \right), \tag{1}$$

$$\frac{\partial u}{\partial x} + \frac{\partial v}{\partial y} = 0, \tag{2}$$

with boundary conditions at the interface and wall

$$y = h(x,t): \quad \frac{\partial u}{\partial y} = 0, \quad v = \frac{\partial h}{\partial t} + u \frac{\partial h}{\partial x}; \tag{3}$$

$$y = 0: \quad u = v = 0. \tag{4}$$

We require only inlet conditions for the flow field in this 'parabolicized' boundary layer equation. They are chosen to be

$$x = 0: \quad h = 1, \quad v = 0, \quad u = u_N(y) \left[1 + \frac{\epsilon}{3} \sum_{n=0}^{100} \cos(n\omega_1 t + \phi_n) \right], \tag{5}$$

where ω_1, the frequency unit, is usually taken to be $1/50$ the neutral frequency of the primary instability–half of the harmonics are unstable and the rest stable. The velocity profile $u_N(y)$ is the parabolic one for a flat film. The constant Fourier amplitude $\epsilon/3$ and a random phase ϕ_n evenly distributed within $[0, 2\pi]$ then constitute white-noise forcing of the flow rate at the inlet. Soft boundary conditions are placed at the exit to minimize upstream feedback (Chang *et al.* 1996a), $\partial h / \partial x = \sigma(h - 1)$ and $\partial^2 h / \partial x^2 = \sigma(\partial h / \partial x)$, where σ is a relaxation parameter taken to be between 0.1 and 2.

One can conveniently expand $u(x, y, t)$ of (1) in a self-similar manner such that the appropriate boundary conditions at (3) and (4) are satisfied:

$$u(x, y, t) = \sum_{k=1}^{K} u_k(x, t)\psi_k(\eta), \tag{6}$$

where $\eta = y/h(x, t)$ and

$$\psi_k(\eta) = \eta^k - \frac{k}{k+1}\eta^{k+1}. \tag{7}$$

If a Galerkin projection is used to determine the equations for the coefficients u_k, the weighting function is η^k. The crudest approximation is with $K = 1$. With $u_1 = 3q/h$, where q is the flow rate, this crudest approximation reduces to Shkadov's (1967) model,

$$\frac{\partial q}{\partial t} + \frac{6}{5}\frac{\partial}{\partial x}\left(\frac{q^2}{h}\right) = \frac{1}{5\delta}\left(h\frac{\partial^3 h}{\partial x^3} + h - \frac{q}{h^2}\right), \tag{8}$$

$$\frac{\partial h}{\partial t} + \frac{\partial q}{\partial x} = 0. \tag{9}$$

The inlet noise amplitude for the flow rate is now ϵ from (5).

Depending on the domain size and the magnitude of δ, we typically utilize $K = 1$ to 4 modes in the Galerkin expansion of the boundary layer equation. A convergence study is carefully carried out to ensure the spatio-temporal dynamics do not change significantly with respect to K (see Chang *et al.* 1996a). We find the required K to increase with δ such that for δ in excess of 2, about $R = 200$ for water, we are unable to reproduce accurate statistics of the wave dynamics of a 2 m long channel (for water) within a practical computation duration (< 1 week) on a workstation. The problem may not be numerical. The Shkadov model and the low-order boundary layer equations are known to produce a poor description of the capillary ripples in front of the pulses at high Reynolds number R (Ruyer-Quil & Manneville 1998). They may be inadequate and may produce inaccurate spatio-temporal dynamics for δ in excess of 2.

A severe limitation of equations (1) and (2) or (8) and (9) is the restriction to two-dimensional waves. Fortunately, due to an extension of Squire's theorem to falling-film waves, two-dimensional waves at inception have been shown to be more unstable than three-dimensional ones (Chang *et al.* 1993). Consequently, if the inlet noise field is sufficiently small in amplitude, linear filtering during wave inception would produce predominantly two-dimensional waves. Alternatively, properly designed wave makers at the inlet can trigger large two-dimensional waves only. Three-dimensional waves will eventually appear downstream even under these conditions. However, they typically develop due to a transverse instability of the two-dimensional pulses. This final transition occurs at a downstream distance that decreases with increasing δ and increasing inclination angle (see the review by Chang 1994). For inclined planes, three-dimensional waves may never appear in a short (< 1 m) channel, as is the case for some of the experiments by Liu & Gollub (1994). Even for the vertical films studied here, much of the pertinent wave coarsening dynamics involving pulses occur prior to the onset of three-dimensional waves at about 40 cm from the inlet for most flow conditions with mild noise (see Stainthorp & Allen 1965, and the review by Chang 1994). This roughly corresponds to $x = 600$. We shall demonstrate that our two-dimensional analysis captures real wave coarsening dynamics by comparing its results to literature data on wave evolution.
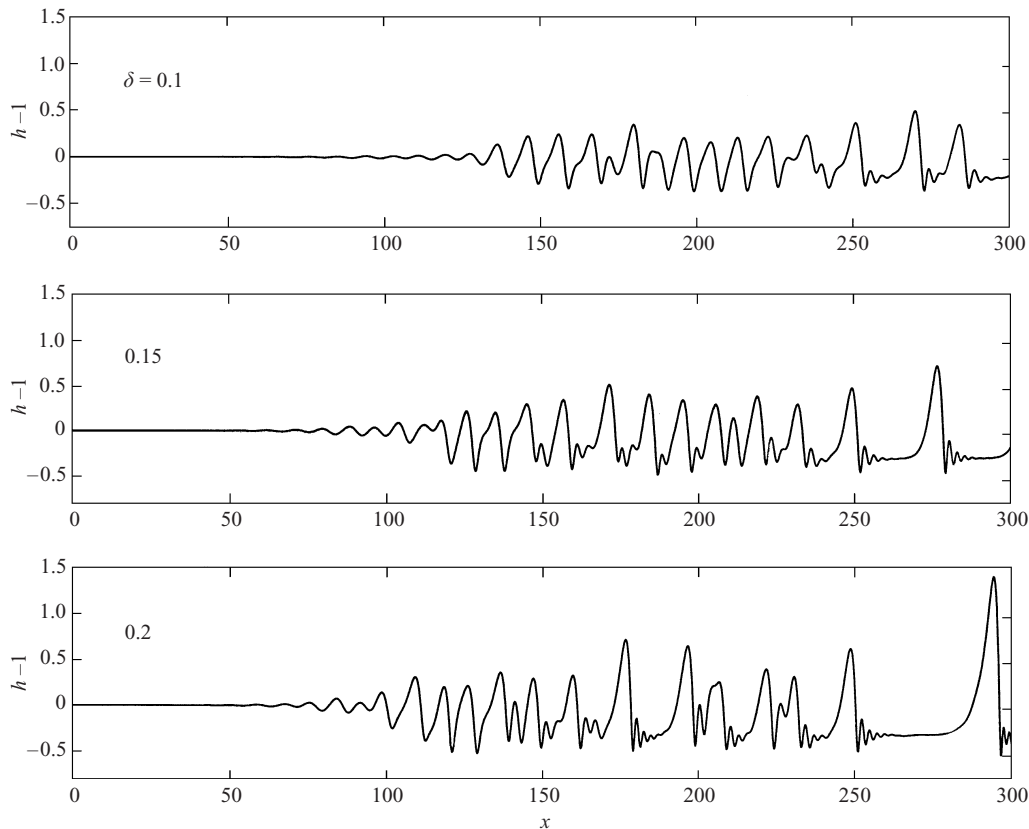
FIGURE 1. Snapshots of wave tracings for three values of δ. White noise of amplitude $\epsilon = 10^{-3}$ is imposed on the flow rate at the inlet $x = 0$.

Snapshots of the waves for $\epsilon = 10^{-3}$ and various values of δ are shown in figure 1. Wave tracings taken at various downstream stations of a typical run are shown in figure 2 for $\delta = 0.1$ and $\epsilon = 10^{-3}$. By $x = 200$, about 14 cm for water, the inlet white noise has been filtered into a modulated wave field whose fundamental frequency is limited to a narrow band around $\omega = \omega_m \sim 1.7$. This is evident in the Fourier spectrum (square root of the power spectrum) of the corresponding wave tracing in figure 3. Also seen in the Fourier spectrum at $x = 200$ are slight overtone $2\omega_m$ and zero-frequency (zero-mode) peaks. These secondary peaks are absent prior to $x = 200$ and hence result from weakly nonlinear interaction with the primary band. The overtone reflects the steepening of the sinusoidal waves as they evolve into pulses.

The modulation frequency is specified by the secondary zero-frequency band. By $x = 280$, this secondary band exhibits a distinct maximum at $\omega = \Delta \sim 0.3$ (see figure 3b). This is the characteristic modulation frequency that is a key to all subsequent wave dynamics. Within a short interval between $x = 225$ and 300 (a 5 cm interval for water), the sinusoidal waves at inception have evolved into solitary pulses (see figure 1). The Fourier spectra of figure 3 reflect this evolution with significant increases in the bandwidths of the fundamental and its overtone. In fact by $x = 300$, these two bands have merged into one, reflecting the large harmonic content of a pulse. As is evident from figure 2(b), abnormally large pulses, larger than the other 'equilibrium' pulses, appear at the nodes of the slow modulation with frequency Δ.
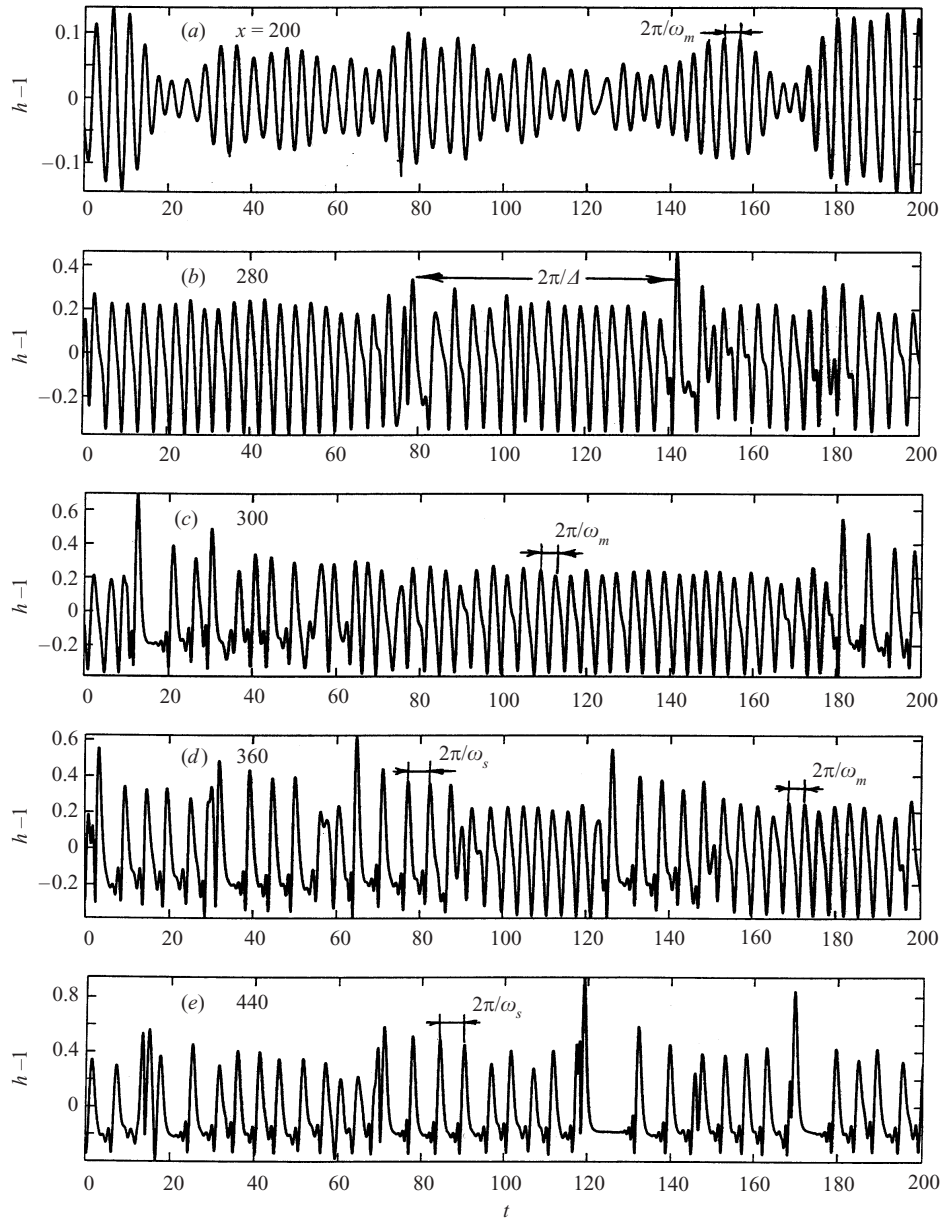
FIGURE 2. Wave tracings measured at stations $x = 200, 280, 300, 360$ and 440 for the noise-driven wave dynamics of figure 1 at $\delta = 0.1$. The initial waves are modulated primary waves of frequency ω_m. Excited pulses form at the dominant modulation period $2\pi/\Delta$ and the pulse separation $2\pi/\omega_s$ increases downstream as the excited pulses eliminate pulses by coalescence. (The specific modulation period shown in (b) for $x = 280$ is $2\pi/\Delta = 60$ but the average at the location shown in the power spectra of figure 3 is $2\pi/\Delta \sim 20$.)

A second peak ω_s appears below ω_m when the pulses are formed and becomes the lone maximum beyond $x = 440$. This ω_s represents the average pulse frequency. The harmonics within this band do not contribute to the shape of individual pulses. As the pulse density decreases downstream, the pulse frequency ω_s decreases, as indicated in figure 3(e).
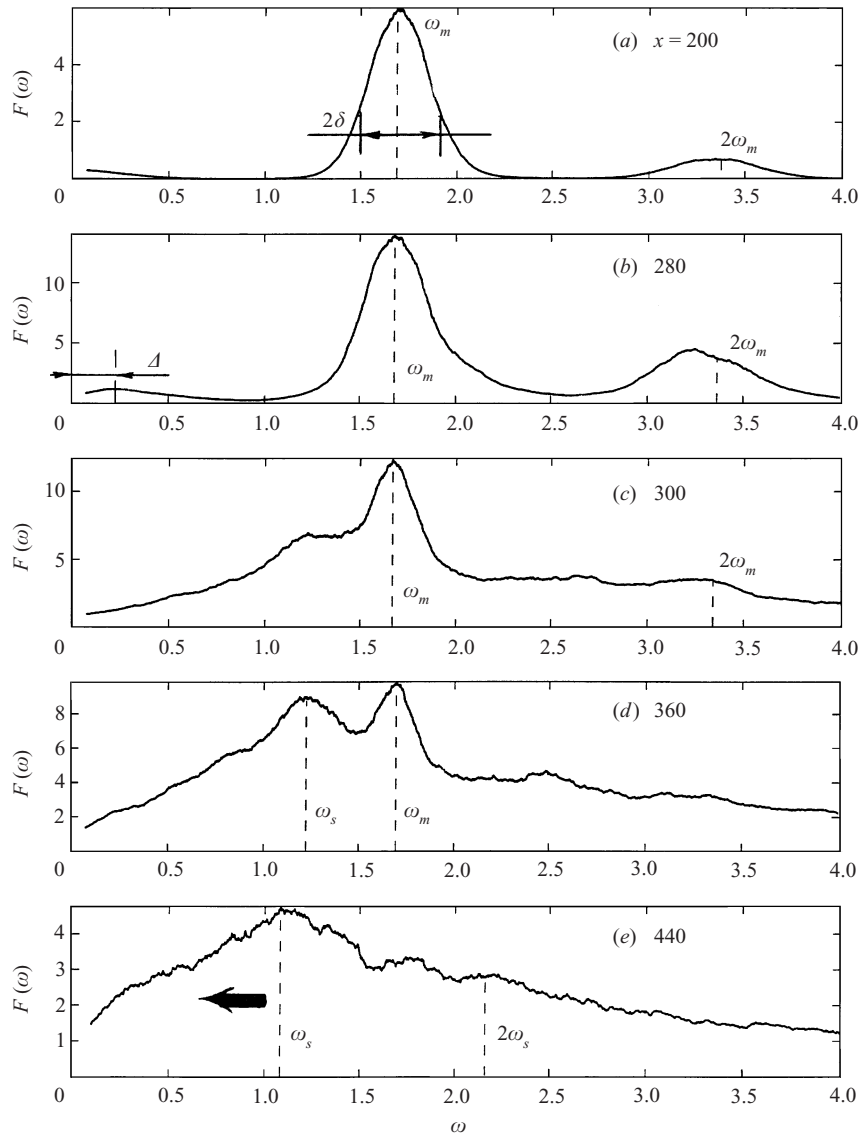
FIGURE 3. Power spectra of the wave tracings in figure 2 with characteristic frequencies ω_m (with standard deviation σ), Δ and ω_s.

The mechanism behind this downstream decrease in pulse density is apparent from the loci shown in figure 4. We call these loci 'world lines' and they track the wave peaks of all waves, both sinusoidal waves and pulses, in the (t, x)-plane. Various intersections are evident as steeper world lines terminate at less steep ones. These correspond to coalescence events that occur when slower pulses (steeper world lines) are captured by faster ones (less steep world lines) from behind (Chang *et al.* 1995, 1996*a*,*b*). Nearly periodic spacing for $x < 200$ corresponds to the filtered band of sinusoidal waves. A dominant frequency ω_m is selected and the resulting nearly monochromatic wave field evolves into equally spaced equilibrium pulses. Some modulation of the primary wave field is evident near $x = 200$ with modulation frequency Δ and the modulation nodes
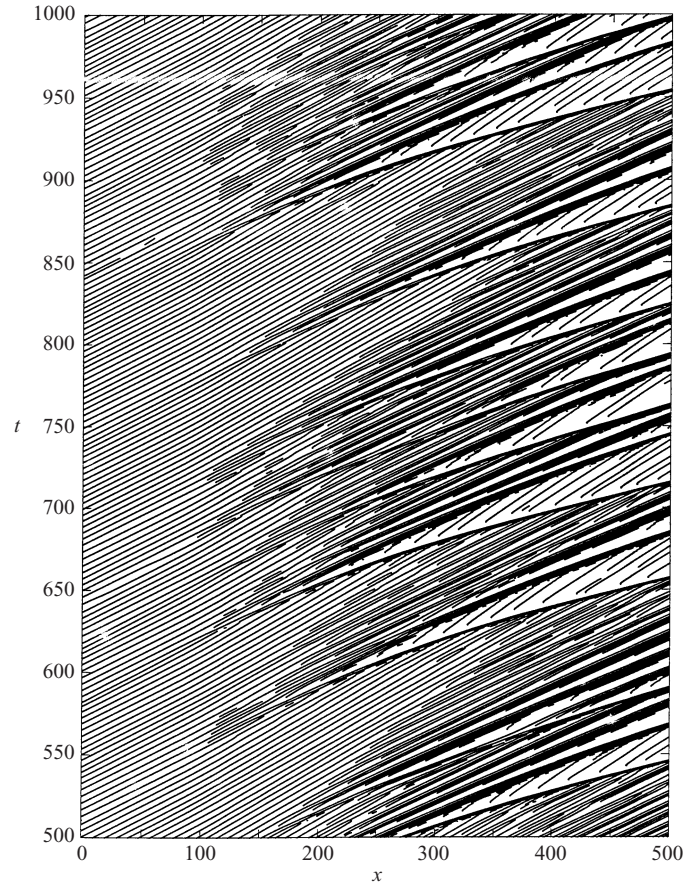
FIGURE 4. World lines tracking the wave crests of noise-driven wave dynamics
in the (t, x)-plane for $\delta = 0.1$.

are seen to produce the 'excited' pulses in figure 2(b). It is clear from figure 4 that these
excited pulses have more inclined world lines than the equilibrium ones, indicating
that they travel faster. They are observed to capture the equilibrium pulses, which
have steeper world lines, downstream. The excited pulses accelerate slowly after each
capture. They survive till the exit of the simulated channel, after all the equilibrium
pulses between the modulation nodes have been captured. A more explicit description
will be offered when wave dynamics driven by a structured inlet noise are presented
in figure 6.

By determining the average spacing in t of the world lines at a given x, we obtain
the average wave period $\langle t \rangle$ at various stations downstream, as shown in figure 5(a).
Except at the onset of coarsening and at the end when the wave period reaches a final
equilibrium value, the wave period is seen to increase downstream, with an almost
linear coarsening rate with respect to x. The noise amplitude ϵ merely determines the
onset location of the coarsening but not its rate nor the final wave period $\langle t \rangle_\infty$. As
is consistent with our earlier observations that the excited pulses are created at the
modulation nodes and that they are the only surviving pulses at the end of the wave
coarsening interval, we find the final wave period to be close to $2\pi/\Delta \sim 20$. (The
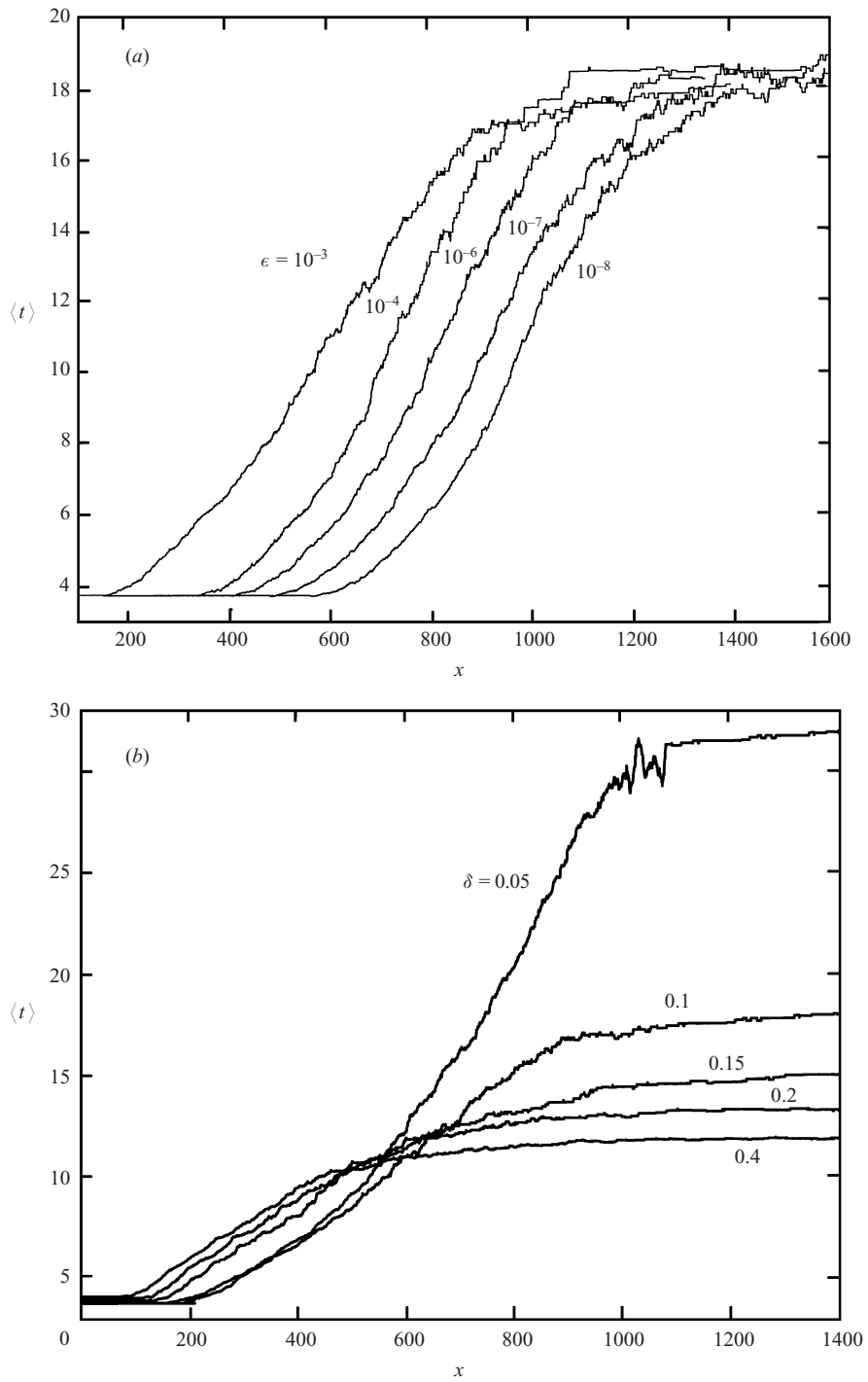value from our simulations in figure 5 is 18.)

FIGURE 5. The average wave/pulse period at each station x for noise-driven wave dynamics for (a) $\delta = 0.1$ and noise amplitude between 10^{-3} and 10^{-8}. (b) $\epsilon = 10^{-3}$ and five different values of δ.
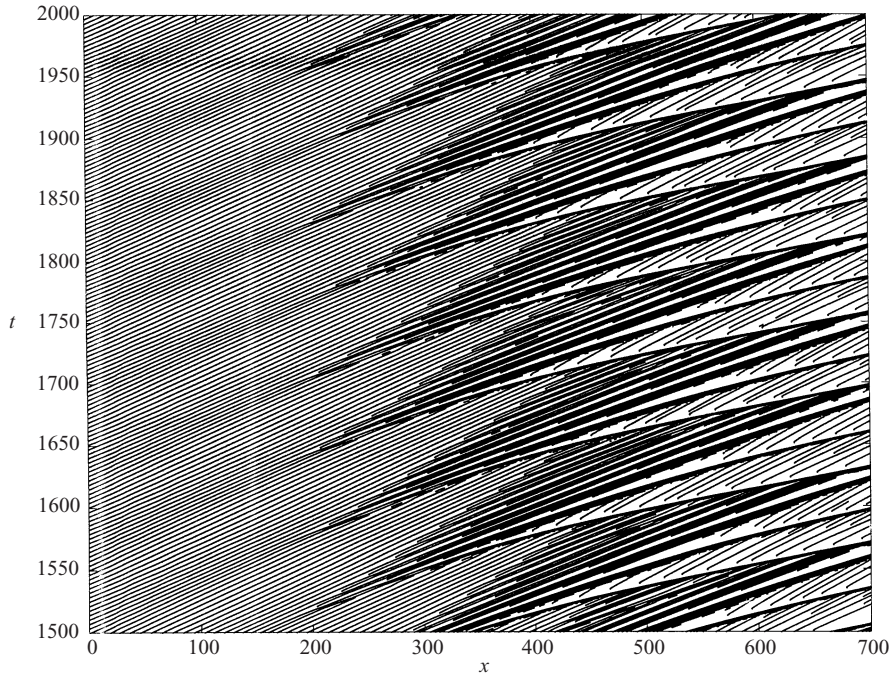
FIGURE 6. World lines with biperiodic forcing at the inlet with a fundamental of $\omega_m = 1.744$, $\delta = 0.1$ and a modulation frequency Δ of 0.1. The dominant excited pulses are clearly created at the modulation minimum at a frequency of Δ.

In figure 5(*b*), we present the wave period coarsening dynamics for a range of δ at the same noise amplitude ϵ. The wave periods within all coarsening intervals show the same linear rate of increase for δ between 0.1 and 0.4. Higher δ values beyond $\delta = 0.4$ are more difficult to simulate and the entire $\langle t \rangle$ profiles cannot be captured. Quite curiously, although δ varies over a large range (water Reynolds number from 10 to 40, the most important practical range) the coarsening rates are nearly constant even though their final wave periods $\langle t \rangle_\infty$ are different. This universal coarsening rate will be a focus of our theoretical and modelling efforts.

This constant coarsening rate breaks down below $\delta = 0.1$ and beyond $\delta = 0.4$. Our visual examination of the simulation displays suggests that, at low δ, the excited pulses do not drain the excess mass after coalescence. The excited pulses hence accelerate downstream, yielding a power-law coarsening rate (with an algebraic power larger than unity) instead of a linear one. This power-law coarsening behaviour is already evident at $\delta = 0.05$ in figure 5(*b*). For δ in excess of 0.4, inertial forces dominate over capillary forces and the excited pulses not only drain their excess mass readily, but they also often break up and form pulses smaller than the equilibrium ones. This consumption of excited pulses reduces the coarsening rate below a linear scaling. As discussed earlier, our model equation may not be valid at high δ and this inertia-driven evolution may be an artifact of our model. It is in the range of 0.05 to 0.4 that the excited pulses remain constant in speed and number, giving rise to universal coarsening dynamics. These invariant properties also render their modelling more feasible. It is fortuitous that this range corresponds to the most practical conditions for industrial falling-film units.

To further ascertain that the characteristic modulation frequency Δ specifies the density of the excited pulses, the coarsening rate and the final wave period, we

introduce periodic forcing with two frequencies – a specific fundamental frequency ω_m and a specific modulation frequency Δ. The primary band and the secondary band hence both become delta functions in the Fourier spectrum. The world lines shown in figure 6 are almost perfectly periodic in time with period $2\pi/\omega_m$ for $x < 200$. This occurs because there are only two frequencies to select during wave inception and the more unstable ω_m dominates over Δ. These primary waves then evolve into equilibrium pulses with the same time spacing $2\pi/\omega_m$. During this evolution of individual wave peaks into pulses, however, the primary wave field also suffers from a modulation instability. Since there is only one modulation frequency Δ available in the noise field, the modulation produces uniformly spaced excited pulses at $x = 200$, in contrast to the irregularly spaced ones in figure 4. At any given station x, the excited pulses arrive at almost the same time intervals of $2\pi/\Delta$. The world lines of these excited pulses have a lower slope, reflecting the higher speeds of the excited pulses, than all pulses upstream of $x = 200$ and all equilibrium pulses between them beyond $x = 200$. They are hence easy to identify. The world line of each excited pulse is seen to extend continuously to the channel outlet but with progressively lower slope (higher speed for the excited pulse) due to the coalescence events. In contrast, the slope of the world lines of the equilibrium pulses remains the same. In fact, these equilibrium world lines terminate when they intersect the world lines of the excited pulses. This indicates that the equilibrium pulses disappear after coalescing with the excited pulses. By the end of our simulation domain at $x = 700$, all the excited pulses created at $x = 200$ still exist and most of the equilibrium pulses have disappeared. There are still some surviving equilibrium pulses between the excited pulses (about four on the average compared to the original 17). However, extrapolation of their trajectories beyond $x = 700$ in figure 6 clearly indicates that they will soon coalesce with the excited pulses. Hence, the excited pulses will be the only remaining pulses far downstream due to these irreversible coalescence events that destroy the equilibrium pulses. Even though considerable distortion of the steeper world lines occurs after each coalescence, corresponding to readjustment of the equilibrium pulses between the excited ones, the excited pulses remain oblivious to such adjustment. They propagate at constant speed between coalescence events and eventually capture all equilibrium pulses. Each surviving pulse at the end can be traced back to a node in the periodic modulation.

In figure 7, we vary the modulation frequency Δ of the biperiodic forcing. It is evident that both the onset of linear coarsening and the rate of coarsening depend on Δ. Moreover, the asymptotic wave period, when coarsening ceases, is almost exactly $2\pi/\Delta$. This is consistent with the observation in figure 6 that the excited pulses with wave period $2\pi/\Delta$ survive the coarsening intact and eventually absorb all the equilibrium pulses. The observed universal coarsening rate in figure 5 for broad-banded noise forcing, which is independent of the noise amplitude ϵ and the flow conditions δ, must hence result when a specific Δ is selected by the wave evolution. The coalescence dynamics must also possess a certain invariance to account for the universality. We seek these invariant features in our subsequent analyses.

Finally, it should be emphasized that the rich wave dynamics on the film are driven by the pulse coherent structures. A naive interpretation of the last power spectrum, shown in figure 3(*e*), measured at $x = 440$, is that it resembles a 'turbulent' spectrum with a power-law 'inertial' tail. The implicit assumption is that the phases of the wave Fourier harmonics are random and the power-law decay is due to a weakly nonlinear energy cascade to higher wavenumbers. This interpretation would be incorrect. As seen in the wave tracing of $x = 440$ in figure 2, the wave harmonics phase lock and
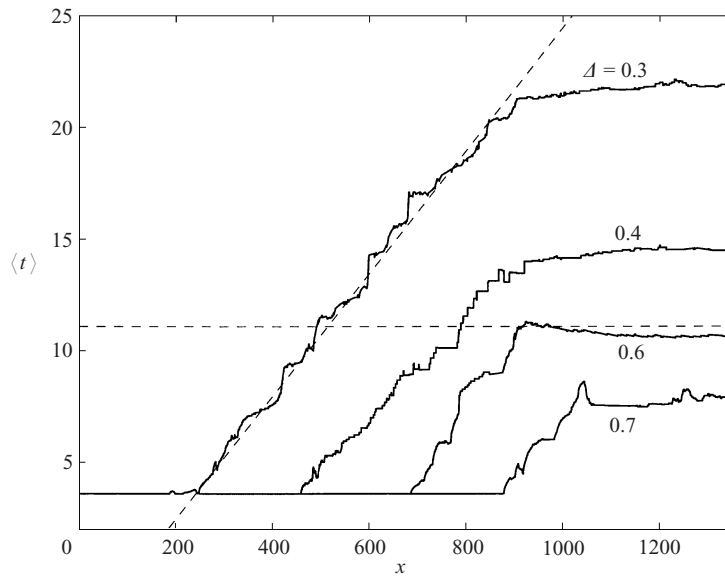
FIGURE 7. Coarsening of average wave period downstream for biperiodic forcing at $\omega_m = 1.744$, $\delta = 0.1$ and the indicated values of Δ.
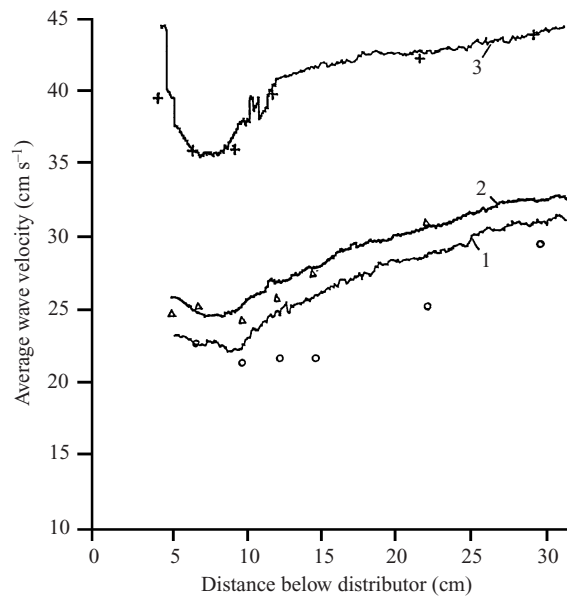

FIGURE 8. Comparison of simulated wave speed evolution compared to values measured by Stainthorp & Allen for water at (1) $R = 15$, (2) $R = 14$ and (3) $R = 31$.

synchronize to form individual solitary pulses. In fact, the power spectrum of each pulse resembles that of the aggregate in figure 3 (omitting the pulse frequency band at ω_s). The absence of phase information in the wave spectrum can hence be misleading and a turbulent spectral theory for thin-film wave dynamics would be misguided. One needs to capture the pulse dynamics to decipher the rich wave dynamics. This coherent structure approach is fundamental to all our work on falling-film waves.

Unfortunately, recorded wave statistics are usually the average wave speed at various downstream stations and not the wave period. To verify the accuracy of our two-dimensional model in capturing the wave coarsening dynamics, we compare in figure 8 our simulated average wave speeds in physical units to the measured ones by Stainthorp & Allen (1965) for water at three Reynolds numbers. The noise Fourier amplitude ϵ has been chosen such that the wave inception length is consistent with the measured value (see Chang *et al.* 1996*a* for details). The pulses are formed at about 10 cm from the inlet (distributor). Their average speed then increases downstream as the pulse density decreases due to coalescence. This reflects the larger fraction of faster excited pulses downstream. It is evident that the simulations are in good agreement with Stainthorp & Allen's measurements. The agreement extends to 30 cm from the inlet where the waves begin show transverse variations in the experiments. Wave coarsening is hence due to two-dimensional wave dynamics even for vertical films that are most susceptible to three-dimensional disturbances.

3. Linear evolution and excitation of low-frequency secondary band

Primary monochromatic waves on an inclined falling film, with frequencies close to that of the maximum-growing one at ω_m, have been shown to be unstable to a modulation (side-band) instability experimentally (Liu & Gollub 1994), numerically (Ramaswamy, Chippada & Joo 1996) and theoretically (Cheng & Chang 1995). We have also carried out a numerical Floquet stability analysis of these dominant monochromatic waves for a vertical film (Chang *et al.* 1993) and have found them to be modulationally unstable.

What is surprising in the current simulation is the existence of a dominant modulation frequency Δ that specifies the density of excited pulses. Due to the translational invariance of the periodic waves, the Floquet growth rate of a monochromatic wave vanishes at zero frequency – it is neutrally stable to infinitely long modulations. Its growth rate then grows as ω^2 from zero frequency and then decays as ω^4 to yield a dominant Floquet mode, provided this is not suppressed by a subharmonic instability (Cheng & Chang 1995). However, the frequency of this dominant mode can be more than three times the observed Δ, suggesting a different mechanism is at play.

These earlier modulation and Floquet theories assume that the low-frequency modulation modes are triggered only after the monochromatic waves have saturated in amplitude. As is evident in figure 3(*a*), a secondary band around a low frequency Δ is already evident at $x = 200$ before the primary band, corresponding to the monochromatic primary wave field, saturates at $x = 280$ when its amplitude ceases to grow. This initial modulation band has a maximum at zero frequency instead of a finite Δ. It is clearly not due to the modulation instability of the saturated primary band, whose dominant frequency is several times higher than Δ.

In our earlier computation of the Landau coefficients of weakly nonlinear interactions responsible for primary wave saturation in a long-wave instability (Cheng & Chang 1995), the zero mode has been shown to participate in the saturation dynamics of the primary monochromatic wave. Comparison to experimentally measured saturated amplitude is only consistent if this zero-mode contribution is included (Sangalli, McCready & Chang 1997). By the slaving principle used in that analysis, this participation of the zero mode also implies that it is quadratically slaved to the primary mode. Hence, a secondary band of low-frequency modes is excited during the growth and saturation of the primary band.

This then suggests that the available modulation modes, excited during the saturation of the primary wave, trigger the subsequent modulation instability of the saturated band, with a growth rate that grows quadratically with the modulation frequency. However, the initial amplitudes of these low-frequency modes are determined by quadratic slaving during primary wave saturation. Moreover, such slaving is expected to produce the largest amplitude at zero frequency where there is no frequency mismatch (Cheng & Chang 1995). The competition between these two opposing behaviours near zero frequency will be shown to produce the selected modulation frequency $\varDelta$. We capture the slaved excitation of the secondary band here and determine $\varDelta$ with a Floquet theory in the next section.

We shall formulate our theory with the simpler Shkadov model (8) and (9), which is quantitatively consistent with the boundary layer equation for δ less than unity. Linearization about the Nusselt basic state $(q, h) = (1, 1)$ yields the dispersion relationships

$$c^2 - c\left(\frac{12}{5} - \frac{i}{5\alpha\delta}\right) + \frac{6}{5} - \frac{\alpha^2}{5\delta} - \frac{3i}{5\alpha\delta} = 0, \tag{10}$$

$$\alpha^4 - (\omega^2 - 12\alpha\omega + 6\alpha^2)\delta + i(3\alpha - \omega) = 0. \tag{11}$$

The first dispersion relationship is for temporal evolution with a real wavenumber α and two complex wave speeds c. The second one corresponds to spatial evolution with a real wave frequency ω and four complex wavenumbers α. We shall focus on spatial evolution and will hence utilize (11). There are, however, four spatial roots α of (11). As shown by Cheng & Chang (1995), only those two spatial modes that propagate downstream are pertinent. Each spatial mode is also associated with a distinct wave speed $c = \omega/\alpha_r$. We denote the two modes as $c_{1,2}$ and $\alpha^{1,2}$ with mode 1 unstable $(-\alpha_i^1 > 0)$ and mode 2 stable $(-\alpha_i^2 < 0)$.

In fact, given the single-harmonic disturbance quantities

$$h - 1 = \hat{h}(x)\exp(i\alpha_r x - i\omega t), \tag{12}$$

$$q - 1 = \hat{q}(x)\exp(i\alpha_r x - i\omega t) \tag{13}$$

for a given frequency ω, since $\hat{h}(0) = 0$ and $\hat{q}(0) = \epsilon$ from (5), solution of the linearized Shkadov model readily yields

$$\hat{h}(x) = \frac{\epsilon}{c_1 - c_2}\exp(-\alpha_i^1 x) - \frac{\epsilon}{c_1 - c_2}\exp(-\alpha_i^2 x). \tag{14}$$

As $x \to \infty$, the stable mode contribution vanishes and

$$\hat{h}(x) = \frac{\epsilon}{c_1 - c_2}\exp(-\alpha_i^1 x). \tag{15}$$

Hence, the inlet flow rate disturbance of amplitude ϵ excites an interfacial mode that extrapolates to the amplitude $\epsilon/|c_1 - c_2| = \epsilon'$ at the inlet – even though there is no interfacial disturbance at the inlet. Our computation of the damping factor $1/|c_1 - c_2|$ shows that it is small for δ less than 0.2 but approaches a constant asymptote 0.25 beyond that value.

The downstream linear evolution of the entire spectrum of harmonics is then

$$\hat{h} = \epsilon' \int_{-\infty}^{\infty}\exp(-i(\omega t - \alpha_r x) - \alpha_i x)\,d\omega, \tag{16}$$

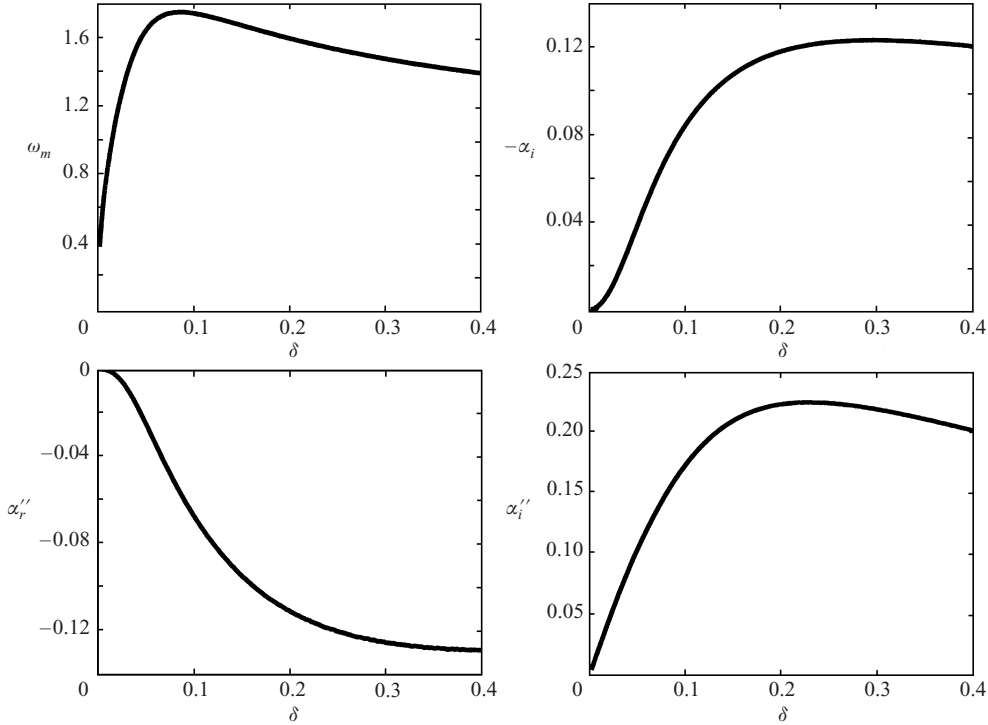where only the unstable first mode is considered now. The interfacial Fourier spectrum

FIGURE 9. The dominant primary frequency ω_m, spatial growth rate α_i and second derivaties of α_r and α_i at ω_m as functions of δ.

of this linear evolution is then

$$F(\omega) = \epsilon' \exp(-\alpha_i(\omega)x). \tag{17}$$

Given the parabolic spatial growth rate of the long-wave instability, this linear evolution will soon filter the white-noise spectrum at $x = 0$ into a sharp Gaussian band

$$F(\omega) \sim \epsilon' \exp(ax - bx(\omega - \omega_m)^2), \tag{18}$$

where $a = -\alpha_i(\omega_m)$, $b = \frac{1}{2}(\partial^2\alpha_i/\partial\omega^2)(\omega_m)$ and ω_m corresponds to the maximum of the growth rate, $(\partial\alpha_i/\partial\omega)(\omega_m) = 0$. Dependence of ω_m, $-\alpha_i(\omega_m)$, $2b = (\partial^2\alpha/\partial\omega^2)(\omega_m)$ and $(\partial^2\alpha_r/\partial\omega^2)(\omega_m)$ of the unstable first mode on δ is shown in figure 9 and in table 1, along with its group velocity $c_g = 1/(\partial\alpha_r/\partial\omega)(\omega_m)$.

With proper normalization, this evolving band is described by the probability density

$$p(\omega) = \sqrt{\frac{bx}{\pi}} \exp(-bx(\omega - \omega_m)^2) \tag{19}$$

with a standard deviation $\sigma = 1/\sqrt{2bx}$ that decays downstream. Both the theoretical Fourier spectrum (19) and the predicted standard deviation evolution are in quantitative agreement with the simulated spectra for $x < 150$ at $\delta = 0.1$ and $\epsilon = 10^{-7}$, as shown in figure 10. The Gaussian approximation becomes increasingly accurate downstream as the broad-banded white noise at the inlet is filtered and focused into a sharp peak in the Fourier spectrum. Beyond $x = 170$, however, nonlinear effects begin

δ	$c_g(\omega_m)$	$\alpha_r''(\omega_m)$	$2b = \alpha_i''(\omega_m)$	ω_m
0.02	2.983	−0.004	0.044	1.151
0.04	2.889	−0.017	0.085	1.539
0.06	2.730	−0.035	0.120	1.703
0.08	2.569	−0.053	0.149	1.748
0.10	2.432	−0.068	0.172	1.744
0.12	2.324	−0.081	0.190	1.720
0.14	2.238	−0.091	0.204	1.689
0.16	2.170	−0.100	0.213	1.658
0.18	2.116	−0.106	0.219	1.628
0.20	2.071	−0.112	0.223	1.599

TABLE 1. Dispersion coefficients of the primary mode.

to corrupt this linear filtering. Overtone and zero-frequency bands appear, as seen in figure 3. The exponential growth downstream is also saturated by this nonlinear interaction.

However, at the initial stage of this transition region, the primary band can still be described by $F(\omega)$ of (18) and we use it to estimate the secondary band $R(\omega)$ at low frequencies. At these low amplitudes, a low-frequency mode of frequency ω is excited by a quadratic interaction between a harmonic of frequency β within the primary band and its sideband of frequency $\omega - \beta$ (see Cheng & Chang 1995 and Sangalli *et al.* 1997). As such the low-frequency secondary band can be approximated by

$$R(\omega) = \int_{-\infty}^{\infty} F(\beta)F(\omega - \beta)\,d\beta, \tag{20}$$

where we have omitted the phase between the harmonics β and $\omega - \beta$. A specific phase relationship exists between the two but we assume that it is independent of ω and β. Thus, (20) is off by a constant independent of ω. Carrying out the Gaussian integral, we obtain an estimate of the secondary band

$$R(\omega) = (\epsilon')^2 \sqrt{\frac{\pi}{2bx}} \exp(2\alpha x - bx\omega^2/2). \tag{21}$$

An important prediction of (21) is that the secondary band near zero frequency has a standard deviation that is $\sqrt{2}$ higher than the primary band. This is consistent with our simulated spectra. In fact, by determining the missing constant (0.03) from the height of the secondary spectra at $x = 140$, our estimate (21) is able to quantitatively capture all zero-frequency secondary bands downstream, as seen in figure 11. The agreement improves downstream as the stable linear modes have become negligible in amplitude and no longer participate through quadratic interaction to the dynamics of the primary band and as nonlinear excitation of the secondary band becomes more pronounced with larger amplitudes in the primary band. This agreement empirically verifies our phase approximations in (20). This low-frequency secondary band provides the initial noise for the modulation instability of the saturated primary wave field downstream, as is analysed in the next section.

4. A theory for the characteristic modulation frequency

As soon as the fundamental mode with frequency ω_m and the small band of waves around it saturate in amplitude, the excited secondary band of modes near zero
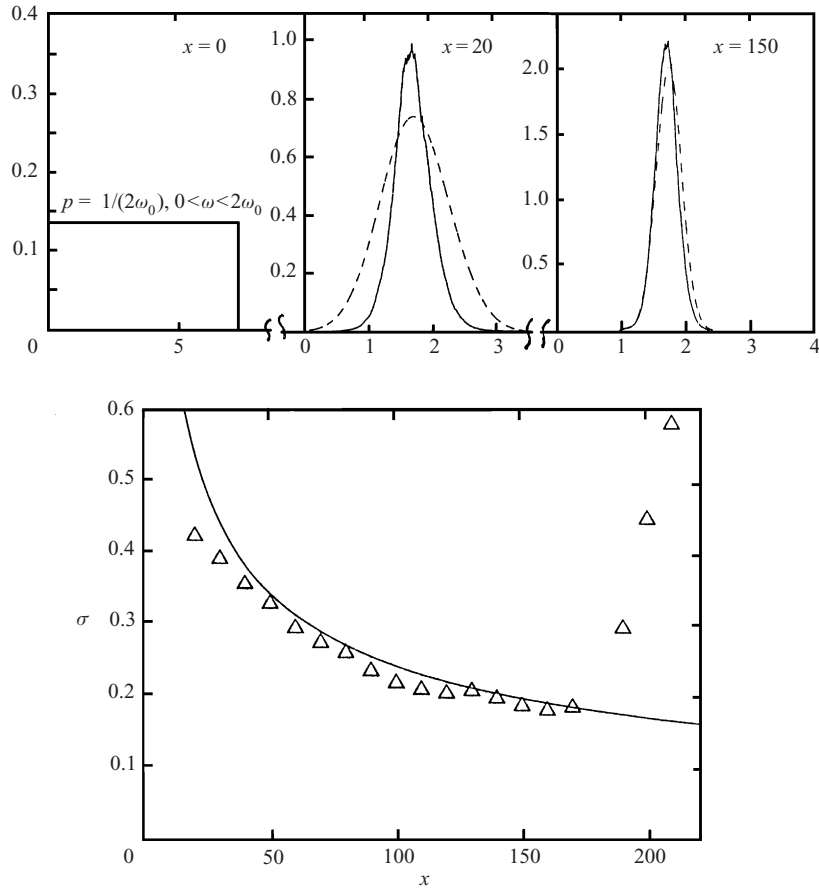
FIGURE 10. Simulated and predicted primary band of waves showing filtering of the initial white spectrum to a narrowing Gaussian with a standard deviation that decreases monotonically as $x^{-1/2}$ downstream at $\delta = 0.1$ and $\epsilon = 10^{-7}$.

frequency in (21) begins to destabilize the primary band by triggering pronounced modulations (see figure 2). This saturation occurs at a distance x_0 from the inlet:

$$x_0 = -\frac{1}{\alpha_i(\omega_m)}\log(r_1/\epsilon'),\tag{22}$$

where $r_1 = |A_1|$ is the amplitude of the saturated fundamental that will be estimated below.

We utilize the technique of Frisch, She & Thual (1986) to construct the saturated periodic solutions of a long-wave instability, including the fundamental mode with r_1, and to examine their modulation instability via an analytical Floquet theory (see also Chang *et al.* 1997, 1999). As primary waves saturate and become stationary travelling waves, they can be described by the Shkadov model (8) and (9) after the moving coordinate transformation $\partial/\partial t = -c\partial/\partial x$,

$$-c\frac{\partial q_0}{\partial x} + \frac{6}{5}\frac{\partial}{\partial x}\left(\frac{q_0^2}{h_0}\right) = \frac{1}{5\delta}\left(h_0\frac{\partial^3 h_0}{\partial x^3} + h_0 - \frac{q_0}{h_0^2}\right),\tag{23}$$

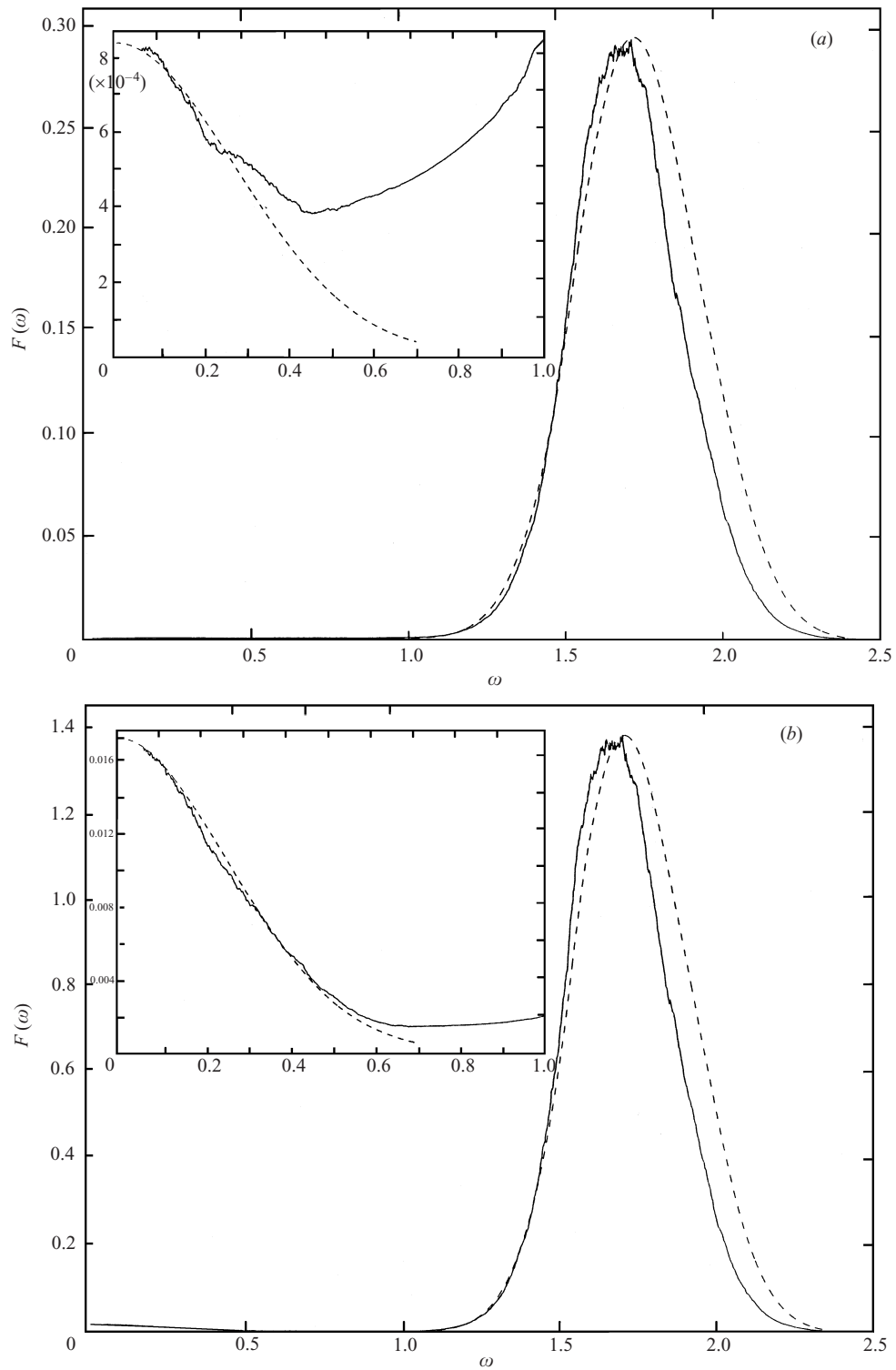$$-c\frac{\partial h_0}{\partial x} + \frac{\partial q_0}{\partial x} = 0.\tag{24}$$

FIGURE 11. The noise-driven primary and slaved secondary bands and our predicted spectra for $\epsilon = 10^{-7}$ and $\delta = 0.1$ at (*a*) $x = 150$ and (*b*) 170.

Integrating the kinematic equation (24) over a patch of periodic travelling waves and assigning the mean thickness for this wave train to be χ, one obtains

$$q_0(x) = ch_0(x) - c\chi + \langle q_0 \rangle. \tag{25}$$

Due to the saturated periodic wave train, the mean thickness χ is different from the flat-film Nusselt thickness ($h = 1$ from our scaling) and the average flow rate $\langle q_0 \rangle$ (over one wavelength of the periodic basic state) does not scale as χ^3, as would be the case for a flat film.

Substituting (25) into (23), we obtain the governing equation for the periodic travelling wave:

$$h_0 \frac{\partial^2 h_0}{\partial x^3} + \delta \left[6(\langle q_0 \rangle - c\chi)^2 - c^2 h_0^2 \right] \frac{\mathrm{d}h_0}{\mathrm{d}x} + h_0^3 - ch_0 - \langle q_0 \rangle + c\chi = 0 \tag{26}$$

with unknowns $h_0(x)$, c and $\langle q_0 \rangle$ at fixed χ, δ and the wavenumber α of the periodic wave.

A closed-form estimate of the solution to (26) can be obtained with a two-harmonic approximation for the profile $h(x)$, where the wavenumber α is within the unstable band,

$$h_0 = \chi + r_1 \cos \alpha x + r_1^2 (A \cos 2\alpha x + B \sin 2\alpha x). \tag{27}$$

Balancing terms for each harmonic, one obtains $c(\alpha, \chi, \delta)$ and $\langle q_0 \rangle(\alpha, \chi, \delta)$ explicitly:

$$\left. \begin{aligned} A &= \frac{3}{15\alpha\delta\chi^5 - 4\alpha^3\chi^2}, & B &= -\frac{3\alpha^2\chi + 18\delta\chi^4}{15\delta\chi^5 - 4\alpha^2\chi^2}, \\ c\alpha &= \omega = 3\alpha\chi^2 - \tfrac{123}{10}r_1^2\alpha, & \langle q_0 \rangle &= \chi^3 + 6r_1^2\chi, \\ r_1^2 &= \frac{\alpha^3\chi^3 - 15\alpha\delta\chi^6}{\kappa}, & \kappa &= -\tfrac{621}{50}\chi\alpha^3 + \frac{18}{30\alpha\delta\chi^4 - 8\alpha^3\chi}. \end{aligned} \right\} \tag{28}$$

This estimate includes an estimate of the amplitude r_1 for the fundamental when the average thickness is unity ($\chi = 1$) or when the average flow rate is unity ($q = 1$). The former condition is closer to the saturated primary waves of our system. However, the full χ dependence must be retained in (28). Unlike the classical modulation instability of short-wave instabilities, the χ dynamics are crucial in the modulation of long-wave instabilities (Frisch *et al.* 1986 and Chang *et al.* 1997). Hence, for the primary wave, (25), (27) and (28) yield the wave field and local flow rate $h_0(x)$ and $q_0(x)$ as functions of χ at fixed wavenumber α and normalized Reynolds number δ.

Consider small perturbations of the basic state, which is any periodic wave within the unstable band:

$$h = h_0(x) + \hat{H}(x, t), \tag{29}$$

$$q = q_0(x) + \hat{Q}(x, t). \tag{30}$$

After substituting into (8) and (9) and linearizing, one obtains the system

$$\frac{\partial \hat{Q}}{\partial t} = b_1 \frac{\partial^3 \hat{H}}{\partial x^3} + b_2 \frac{\partial \hat{Q}}{\partial x} + b_3 \frac{\partial \hat{H}}{\partial x} + b_4 \hat{Q} + b_5 \hat{H}, \tag{31}$$

$$\frac{\partial \hat{H}}{\partial t} = c \frac{\partial \hat{H}}{\partial x} - \frac{\partial \hat{Q}}{\partial x}, \tag{32}$$

where

$$b_1 = \frac{h_0}{5\delta}, \quad b_2 = c - \frac{12}{5}\frac{q_0}{h_0}, \quad b_3 = \frac{6}{5}\frac{q_0^2}{h_0^2},$$

$$b_4 = -\frac{12}{5}\left(\frac{q_0^2}{h_0^2}\right)' - \frac{1}{5\delta h_0^2}, \quad b_5 = \frac{6}{5}\left(\frac{q_0^2}{h_0^2}\right)' + \frac{1}{5\delta}\left(h_0''' + 1 + \frac{2q_0}{h_0^3}\right),$$

and prime denotes derivative with respect to x.

As first shown by Frisch *et al.* (1986) and extended by Chang *et al.* (1999), the dynamics of the disturbances $\hat{Q}$ and $\hat{H}$, as determined by (31) and (32), are dominated by two physical symmetries – the translational symmetry of the periodic wave basic state and a peculiar 'kinematic' symmetry that relates the speed change of the periodic wave to a change in the mean thickness χ. Due to these symmetries, disturbances with long wavelengths are determined by two coupled neutral modes.

Due to the separation of time scales offered by the neutrality of these modes and the separation of length scales offered by their long wavelengths relative to that of the basic state, a two-scale expansion can be carried out for long disturbances by using the ratio v of the basic-state wavelength to the disturbance wavelength as a parameter,

$$\frac{\partial}{\partial x} \rightarrow \frac{\partial}{\partial x} + v\frac{\partial}{\partial x_1}, \quad \frac{\partial}{\partial t} \rightarrow v\frac{\partial}{\partial \tau_1} + v^2\frac{\partial}{\partial \tau_2}. \tag{33}$$

The solution to (31) and (32) can then be expressed as

$$\begin{pmatrix} \hat{Q} \\ \hat{H} \end{pmatrix} = A(x_1, \tau_1, \tau_2)\begin{pmatrix} q_0' \\ h_0' \end{pmatrix}, \tag{34}$$

where q_0' and h_0' are derivatives of q_0 and h_0 with respect to x and they represent the translational mode.

Leading-order expansion then yields the dominant modulation equation (see Chang *et al.* 1998 for a related calculation, and details can be obtained from the authors upon request)

$$a_{11}\frac{\partial^2 A}{\partial \tau_1^2} + 2a_{12}\frac{\partial^2 A}{\partial \tau_1 \partial x_1} + a_{22}\frac{\partial^2 A}{\partial x_1^2} = 0, \tag{35}$$

where

$$a_{11} = -\frac{\partial \langle h_0 \rangle}{\partial \chi}\bigg/\frac{\partial c}{\partial \chi},$$

$$2a_{12} = \alpha\frac{\partial \langle h_0 \rangle}{\partial \alpha} + \left[-\alpha\frac{\partial c}{\partial \alpha}\frac{\partial \langle h_0 \rangle}{\partial \chi} + c\frac{\partial \langle h_0 \rangle}{\partial \chi} - \frac{\partial \langle q_0 \rangle}{\partial \chi}\right]\bigg/\frac{\partial c}{\partial \chi},$$

$$a_{22} = \alpha\left(\frac{\partial \langle q_0 \rangle}{\partial \alpha} - c\frac{\partial \langle h_0 \rangle}{\partial \alpha}\right) - \alpha\frac{\partial c}{\partial \alpha}\left(\frac{\partial \langle q_0 \rangle}{\partial \chi} - c\frac{\partial \langle h_0 \rangle}{\partial \chi}\right)\bigg/\frac{\partial c}{\partial \chi},$$

and $\langle \ldots \rangle$ denotes integration over one wavelength of the basic state. All derivatives can be evaluated from (27) and (28) at the basic state values.

We are particularly interested in the frequencies and Floquet growth rates of the modulation waves triggered by the dominant primary wave within the primary band. This wave has a frequency ω_m and a wavenumber $\alpha_m = (\omega_m/c)$. These values are inserted into (35). Using a normal mode $\exp(\mu\tau_1 + ix_1)$ solution of (35), the Floquet eigenvalues μ specifying the growth rates of the modulation modes are determined

δ	a_1	a_2	a_3	a_4
0.02	0.0182	0.130	0.0226	-0.190
0.04	0.1167	0.468	0.2074	-0.731
0.06	0.2076	0.857	0.5656	-1.714
0.08	0.2430	1.204	1.1311	-2.762
0.10	0.2413	1.501	1.6967	-4.135
0.15	0.1593	2.057	3.1860	-9.001
0.20	0.1110	3.154	5.1617	-14.06

TABLE 2. Secondary Floquet coefficients of the fundamental periodic wave.

by the characteristic polynomial

$$a_{11}\mu^2 + 2a_{12}\mu + a_{22} = 0. \tag{36}$$

Omitting the stable root μ and rescaling the other by the small modulation wavenumber v to obtain the Floquet growth rate in the original unscaled time and spatial coordinates, after an even higher order expansion beyond (35), we obtain

$$\tilde{\mu} = v\mu \sim \mathrm{i}a_1\omega + a_2\omega^2 + \mathrm{i}a_3\omega^3 + a_4\omega^4, \tag{37}$$

where $\omega = c_g v$ is the modulation frequency and c_g is the group velocity of the fundamental mode with frequency ω_m. Strictly speaking, the slow modulation disturbance of a primary periodic wave only travels with a group velocity at the frequency of the primary wave if the primary wave is of small amplitude (Cheng & Chang 1995). Although our primary periodic wave is of finite amplitude, the amplitude is small and we find $c_g(\omega_m)$ to be a good approximation that is accurate within 10%. In table 2, we tabulate the computed coefficients a_i for the dominant (fundamental) primary wave with frequency ω_m of table 1.

The Floquet growth rate determines how the fully grown (saturated) primary wave field drives the modulation waves. However, the initial amplitudes of these modulation waves are determined by the secondary band of (21), which results due to weakly nonlinear interaction of the evolving primary field upstream. Since the modulation packet travels with the group velocity c_g of table 1, the spatial evolution of the secondary band (21), due to the modulation instability with Floquet growth rate (37), is represented by

$$R(\omega) = R_0 \sqrt{\frac{\pi}{2bx}} \exp(-bx_0\omega^2/2) \exp[(a_2\omega^2 + a_4\omega^2)(x - x_0)/c_g], \tag{38}$$

where R_0 is a normalization constant and x_0 is the location (22) where the primary fundamental has saturated.

This spectrum begins with a maximum at $\omega = 0$ for x below a critical value x_1:

$$\frac{x - x_0}{x_0} < \frac{c_g b}{2a_2} = \frac{x_1 - x_0}{x_0}. \tag{39}$$

This critical latent distance x_1 is typically less that $1/10$ of x_0. Beyond this latent distance, the maximum takes on a finite value in ω which increases downstream. This dominant modulation frequency due to a competition between the initial slaving
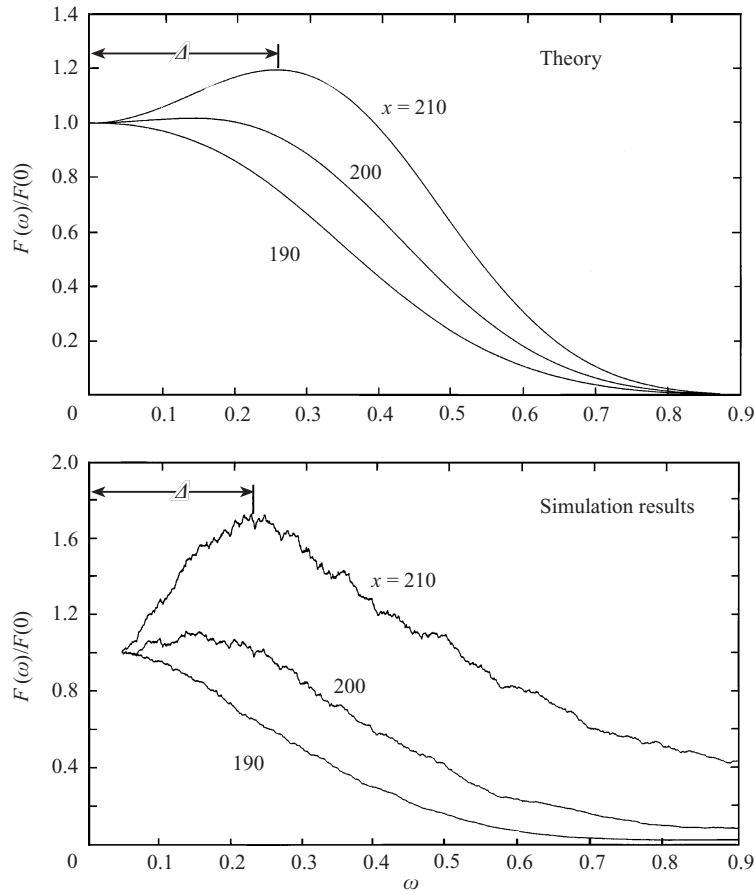
FIGURE 12. The normalized secondary band after the onset of modulation instability with the saturation of the primary band. Both simulation and theory show a dominant modulation frequency Δ for $\delta = 0.1$ and $\epsilon = 10^{-7}$. The onset of modulation is estimated to be $x_0 = 180$.

excitation and the subsequent Floquet instability of the primary wave is then

$$\Delta = \left[\frac{bc_g(x_0/(x - x_0)) - 2a_2}{4a_4} \right]^{1/2}. \tag{40}$$

The theoretical prediction (38) of the secondary spectrum and the predicted maximum modulation frequency (40) are seen to be in good agreement with the simulation results in figure 12 for $190 < x < 210$ beyond $x_0 = 180$ for that case. We note that the dominant modulation frequency predicted by the Floquet growth rate (37) is $(-a_2/2a_4)^{1/2}$. Hence, the first term in (40) corresponds to the correction of the dominant modulation frequency by the initial spectrum of the secondary modulation band (21). At low δ, the correction is significant. For $\delta = 0.05$, for example, the prediction from the Floquet growth rate is larger than the observed value by a factor of 4.

The transition to pulses occurs when the dominant modulation with frequency Δ reaches an amplitude comparable to the amplitude of the fundamental wave r_1 in (22) and (28). It remains unclear how the modulation synchronizes all the harmonics to form a pulse at its nodes but this process is quite apparent in figure 2(*b*).

These first pulses are larger than those created later and hence become the excited pulses. After their creation, very fast phase synchronization dynamics occur at the wave field between them, eventually converting all remaining sinusoidal waves into solitary pulses. These later pulses are almost identical in amplitude and constitute the equilibrium pulses. The earlier excited pulses are larger and begin to overtake and absorb the equilibrium pulses irreversibly, as seen in the last few frames of figure 2 and in the world lines of figure 4.

The density of the equilibrium pulses is approximately ω_m, as each sinusoidal peak at inception is converted to an equilibrium pulse. The density of the excited pulse, however, is determined by the value of Δ when they are first created. We estimate this position x_2 by assuming a linear growth of the dominant modulation until its amplitude reaches the amplitude r_1 of the fundamental

$$a_0 \exp\left(\int_{x_0}^{x_2} \frac{\mu_r}{c_g}\, \mathrm{d}x \right) = r_1, \tag{41}$$

where a_0 is the initial amplitude of the modulation. Substitution of the Floquet growth rate (37) into (41) yields the following transcendental equation for x_2:

$$x_2 - x_0 = \frac{\Gamma_2}{\Gamma_1} x_0 \log\left(1 + \frac{x_2 - x_0}{x_1 - x_0} \right) + \frac{1}{\Gamma_1} \log \frac{r_1}{a_0}, \tag{42}$$

where

$$\Gamma_1 = \left(-\frac{a_2^2}{2 c_g a_4} \right) \quad \text{and} \quad \Gamma_2 = \left(-\frac{b a_2}{4 a_4} \right).$$

In some cases, $x_2 - x_0$ is small compared to $x_1 - x_0$ and an explicit estimate can be obtained:

$$\frac{x_2 - x_0}{x_1 - x_0} = \sqrt{\frac{2}{\Gamma_2 x_0}} \log\left(\frac{r_1}{a_0} \right). \tag{43}$$

We are unable to estimate the initial modulation amplitude a_0 at x_0 – the unknown constant in (21) and (38) for the secondary band prevents an accurate estimate. However, comparison to our numerical values of x_1 and x_2 suggest that a_0 ranges from $0.1 r_1$ to $0.25 r_1$. We use these two limits to estimate a bound for x_2 from (42). These bounds are then inserted into (40) to obtain Δ_2, the dominant modulation frequency at x_2, when the pulses are created. From our simulations, $2\pi/\Delta_2$ also represents the average time interval between excited pulses. As seen in figure 13, these bounds are in good agreement with the simulated pulse frequency at inception for a range of noise amplitude ($\epsilon' = 10^{-8}$ to 10^{-5}) and a range of δ up to unity. In essence, the initial pulse density is almost independent of the white-noise amplitude over this large range of ϵ'. This insensitivity only breaks down after ϵ' exceeds 10^{-3}. We note that the Δ_2 dependence on δ in figure 13(a) resembles that of ω_m in figure 9. As a result, when Δ_2 is divided by ω_m to produce the excited pulse fraction at inception, figure 13(b) shows an almost constant fraction beyond $\delta = 0.10$ that is in good agreement with our simulation results. About one out of every four pulses is excited for δ in excess of 0.1 and about one out of ten is excited for δ less than 0.1. These seem to be robust, universal numbers that are insensitive to noise, provided it is small, and independent of operating fluids/conditions. Not coincidentally, the universal coarsening rate observed in figure 5(b) commences at $\delta = 0.1$. For water, flow conditions below $\delta = 0.1$ correspond to very thin films at Reynolds numbers less than 10. These conditions are dominated by capillary forces and seem to have
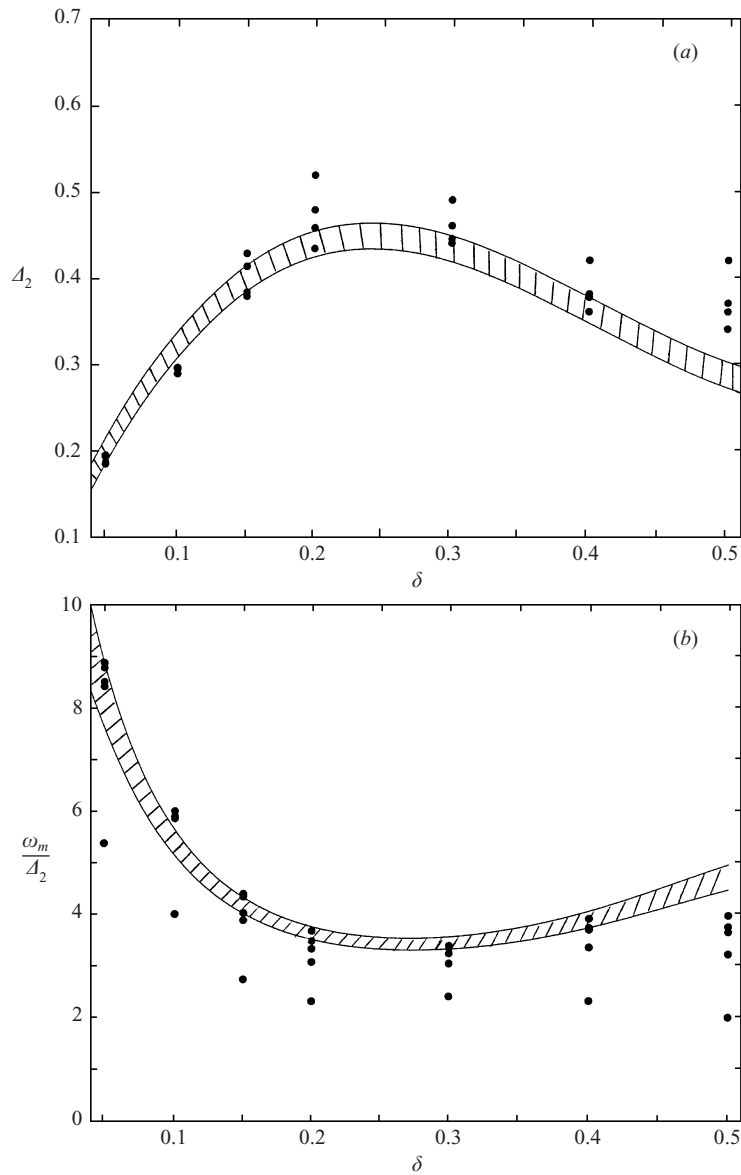
FIGURE 13. (a) The predicted band of excited pulse frequency Δ_2 compared to simulation results. (b) The relative density of equilibrium to excited pulses from simulations compared to the theoretical band ω_m/Δ_2. The numerical results correspond to $\epsilon = 10^{-3}, 10^{-4}, 10^{-5}, 10^{-6}$ and 10^{-7}.

distinctively different dynamics. For the more practical conditions of $\delta > 0.1$, the constant asymptote of Δ_2/ω_m is one key to the universal coarsening rate seen in figure 5.

5. Universal coarsening rate based on Δ

With an estimate for the excited pulse fraction and the average time interval between excited pulses from Δ_2, we are now in a position to quantify the dynamics of pulse coarsening seen in figure 5 – the dominant dynamics of pulses on a falling film. In the
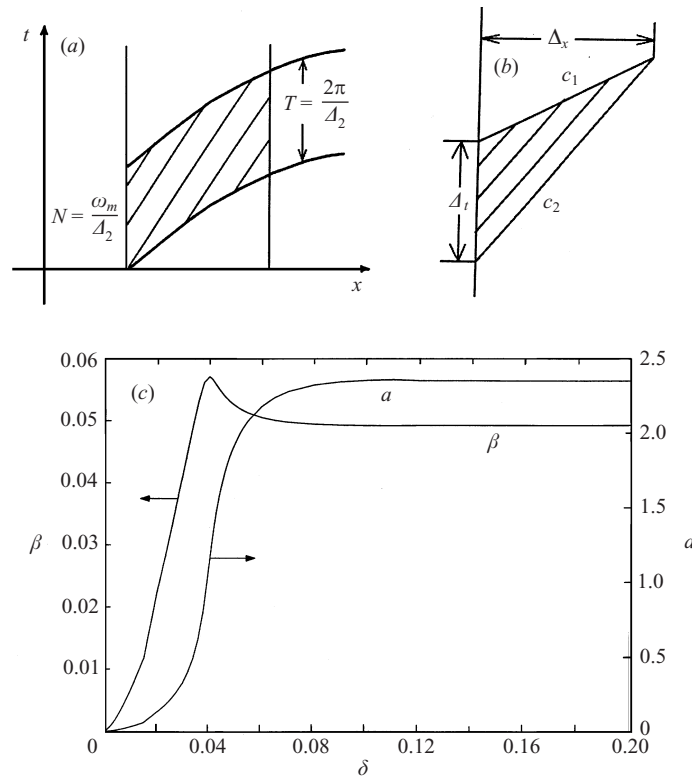
FIGURE 14. (a, b) Schematic for the pulse coalescence model and (c) the equilibrium pulse amplitude a and differential speed between excited and equilibrium pulses β as functions of δ. Since the equilibrium pulse amplitude a reaches a constant asymptote at large δ, the differential speed β between excited and equilibrium pulses also approaches a constant asymptote.

schematics of figure 14, the two thick envelope world lines in figure 14(a) correspond to two excited pulses. On the average, these two excited pulses are separated by a time interval of $T = 2\pi/\Delta_2$ as shown. The thin world lines between these two thick envelopes correspond to equilibrium pulses. Again, in the schematic of figure 14(a) of an 'average' arrangement, there are $N = \omega_m/\Delta_2$ such equilibrium pulses between the excited ones. As seen by the parallel lines of the excited and equilibrium pulses with different slopes, we neglect the adjustment dynamics of the equilibrium pulses and the complex pulse coalescence and mass drainage dynamics at the excited pulses. Instead, we assume the excited and equilibrium pulses all travel at speeds that remain constant for the entire flow domain. This assumption is consistent with the world lines of figures 4 and 6. This implies that the liquid acquired by an excited pulse during a coalescence event is roughly equal to the mass it drains out before the next event. Thus, the average speed of the excited pulse between events is constant over the entire flow domain. This occurs only for relatively fast drainage. For drop coalescence on a thin vertical wire, we find that the excited drops retain much of the mass after each coalescence (Chang & Demekhin 1999). As a result, these drops accelerate downstream and the coalescence frequency also increases monotonically. This scenario seems to occur for $\delta < 0.1$ and will not be modelled here.

Let c_1 and c_2 be the speeds of the excited and equilibrium pulses, respectively. Consider a vertical line parallel to the t-axis shown in figure 14(b). An excited pulse

and an equilibrium one pass this station in space at different times within an interval Δt. If these two pulses coalesce at a different spatial station Δx downstream, the following must be true from simple geometric arguments obvious from figure 14(*b*):

$$\Delta t = \frac{\Delta x}{c_2} - \frac{\Delta x}{c_1} \tag{44}$$

or in differential form

$$\frac{\mathrm{d}t}{\mathrm{d}x} = -\beta = -\frac{c_1 - c_2}{c_1 c_2}. \tag{45}$$

The negative sign of $(\mathrm{d}t/\mathrm{d}x)$ indicates that all the equilibrium pulses within the time interval $\mathrm{d}t$ have been eliminated over a distance of $\mathrm{d}x$. The differential number of equilibrium pulses within this differential period $\mathrm{d}t$ is

$$\mathrm{d}n = \mathrm{d}t \left(\frac{\omega_m}{2\pi} \right) \tag{46}$$

and hence

$$\mathrm{d}n = -\left(\frac{\beta \omega_m}{2\pi} \right) \mathrm{d}x. \tag{47}$$

Integrating from the pulse inception location x_2, one obtains

$$n(x) = n_0 + \frac{\beta \omega_m}{2\pi}(x_2 - x)$$

$$= \frac{\omega_m}{\Delta_2} + \frac{\beta \omega_m}{2\pi}(x_2 - x). \tag{48}$$

Since we have only considered one excited pulse, $n(x)$ is the number of equilibrium pulses between two excited pulses. The average pulse period is then

$$\langle t \rangle = \frac{2\pi/\Delta_2}{n(x)} = \frac{2\pi}{\omega_m + (\beta \omega_m \Delta_2/2\pi)(x_2 - x)}$$

$$\sim \frac{2\pi}{\omega_m} + \left(\frac{\Delta_2}{\omega_m} \right) \beta(x - x_2). \tag{49}$$

The coarsening rate is then

$$\frac{\mathrm{d}\langle t \rangle}{\mathrm{d}x} \sim \left(\frac{\Delta_2}{\omega_m} \right) \left(\frac{c_1 - c_2}{c_1 c_2} \right). \tag{50}$$

The linear correlation between excess pulse speed and excess amplitude has been verified experimentally (Alekseenko *et al.* 1994) and has been captured by our earlier weighted spectral theory for pulses (Chang *et al.* 1995*a*) that utilizes resonance poles. In the present variables, it appears as

$$c \simeq 3.0 + 2.0a, \tag{51}$$

where a here is the total pulse amplitude instead of the excess one. At $a = 0$, one obtains the phase velocity of low-δ sinusoidal waves at inception. Equilibrium pulse amplitude a as a function of δ has been computed in (Chang *et al.* 1995*a*, 1996*b*) and is shown in figure 14(*c*).

We have estimated the excited pulses to have roughly twice the mass of the equilibrium ones owing to the coalescence events (Chang *et al.* 1995*a*, 1996*b*). Since the pulse width remains the same, the excited pulse should also be twice as large
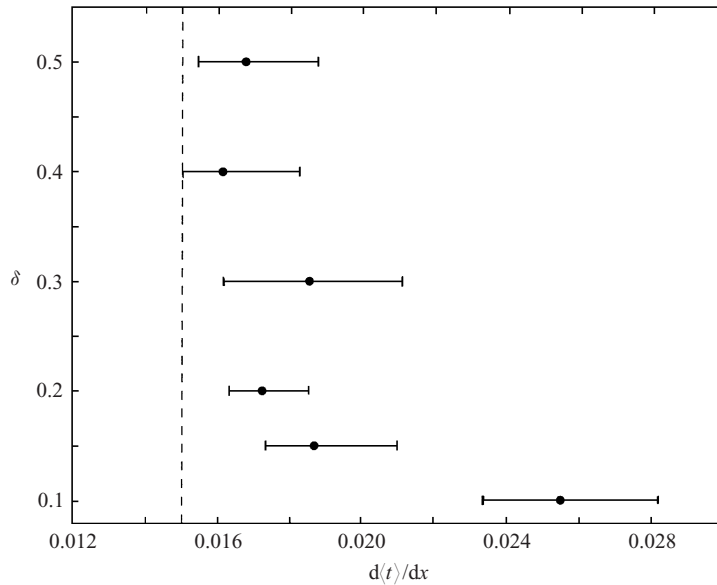
FIGURE 15. The constant asymptote of β beyond $\delta = 0.1$ produces a universal dimensionless coarsening rate $\mathrm{d}\langle t \rangle / \mathrm{d}x = 0.015$ that is consistent with our simulation results. The error bars correspond to noise amplitudes $10^{-7} < \epsilon < 10^{-3}$.

in amplitude. Using this assumption and correlation (51), the parameter β can be expressed in terms of the amplitude of the equilibrium pulse a,

$$\beta = \frac{c_1 - c_2}{c_1 c_2} = \frac{2a}{(3 + 2a)(3 + 4a)}. \tag{52}$$

As shown in figure 14(*c*), for the large pulses beyond $\delta = 0.1$ (*a* larger than 2), this parameter approaches roughly a constant of about 0.05. Combining this universal pulse differential speed with the generic excited pulse fraction of 1/4 for δ larger than 0.15 in figure 13(*b*), we obtain the universal dimensionless coarsening rate

$$\frac{\mathrm{d}\langle t \rangle}{\mathrm{d}x} = 0.015. \tag{53}$$

This rough estimate is in agreement with all our numerical simulations of δ between 0.1 and 0.4 and a wide range of noise amplitudes, as seen in figure 15. In dimensional form, this universal coarsening rate is simply 0.015 divided by the Nusselt average flat-film velocity $\langle u \rangle$.

In figure 16, the final saturated wave period $\langle t \rangle_\infty$ from our simulation, after the coalescence events have ceased, is favourably compared to the theoretical prediction $2\pi / \Delta_2$ from (40) and (43) and from figure 13(*a*). This confirms that only the excited pulses remain at the end and all the equilibrium pulses have been eliminated. This was also the case in figure 7 where the biperiodic forcing imposes a specific modulation frequency Δ. For the broad-banded noise here, the asymptotic wave period far downstream actually corresponds to the modulation frequency selected by the primary and secondary instabilities of inception waves within $x < 200$ (less than 15 cm for water) of the inlet! The dominance of pulse coherent structures and the creation of excited pulses from secondary modulation instability lead to this simple unique feature despite the complex noise-driven wave dynamics.
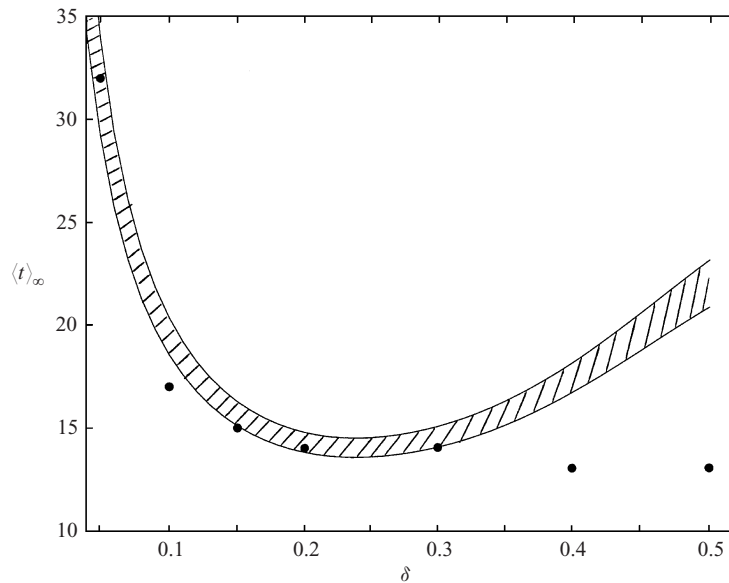
FIGURE 16. The final equilibrium pulse period of figure 5 compared to the theoretical band $2\pi/\Delta_2$.

6. Summary and discussion

A universal coarsening rate of 0.015 independent of noise amplitude ($\epsilon' < 10^{-3}$) and flow conditions ($0.1 < \delta < 0.4$) is a welcome generic conclusion to such a complex hydrodynamic problem. Even more attractive is the observation that this coarsening rate only depends on the dominant modulation frequency Δ and the excited pulse dynamics. The former quantity can be estimated from a relatively simple weakly nonlinear theory, as we have done here, and the latter can also be readily estimated numerically, experimentally or theoretically using resonance pole spectral theory. It is conceivable that this scenario is common to many open-flow hydrodynamic systems with a long-wave instability and localized coherent wave structures. As a result, their wave dynamics can also be deciphered in the same manner. Application to short-wave instabilities with a finite critical wavenumber may also be possible if solitary pulses are possible wave structures in these instabilities. There is some indication that this may be the case if the short waves interact with stable long waves as in two-layer couette flow (Chang *et al.* 1999; Charru & Barthelet 1999).

In a subsequent paper, we shall examine the subcritical ($\delta < 0.1$) and supercritical ($\delta > 0.4$) power-law coarsening rates with a more elaborate model than the Shkadov model and the low-order Galerkin expansion of the boundary layer equation. The remaining unsolved wave dynamics on a falling film would then be the breakup of the solitary pulses into localized three-dimensional wave structures (scallop waves). The spatial location for this transition and its dependence on noise amplitude ϵ and flow conditions δ is currently being investigated by our group. The transverse instability of pulses that triggers the onset of scallop waves is expected to be very sensitive to the capillary ripples in front of the pulses. Once again, such ripples may not be accurately described by the Shkadov model, (8) and (9), or a low-order expansion of the boundary layer equation, (1) and (2). More advanced models, like those offered by Ruyer-Quil & Manneville (1998), may be necessary. However, due to their localized structure on a two-dimensional free surface, these scallop

waves tend not to coalesce and change their density. Consequently, the onset of scallop wave formation and their characteristic size at inception may complete the quantification of all pertinent dynamics and length scales for wave evolution on the falling film.

REFERENCES

ALEKSEENKO, S., NAKORYAKOV, V. & POKUSAEV, B. 1994 *Wave Flow of Liquid Films*, p. 314. Begel House, Inc.

CHANG, H.-C. 1994 Wave evolution on a falling film. *Annu. Rev. Fluid Mech.* **26**, 103.

CHANG, H.-C. & DEMEKHIN, E. A. 1999 Coalescence cascade towards drop formation. *J. Fluid Mech.* **380**, 233.

CHANG, H.-C., DEMEKHIN, E. A. & KALAIDIN, E. N. 1996a Simulation of noise-driven wave dynamics on a falling film. *AIChE J.* **42**, 1553.

CHANG, H.-C., DEMEKHIN, E. A. & KALAIDIN, E. N. 1995a Interaction dynamics of solitary waves on a falling film. *J. Fluid Mech.* **294**, 123.

CHANG, H.-C., DEMEKHIN, E. A. & KALAIDIN, E. 1998 Generation and suppression of radiation by solitary pulses. *SIAM J. Appl. Maths* **58**, 1246.

CHANG, H.-C., DEMEKHIN, E. A. & KOPELEVICH, D. I. 1993 Nonlinear evolution of waves on a vertically falling film. *J. Fluid Mech.* **250**, 433.

CHANG, H.-C., DEMEKHIN, E. A. & KOPELEVICH, D. I. 1995b Stability of a solitary pulse against wave packet disturbance in an active medium. *Phys. Rev. Lett.* **75**, 1747.

CHANG, H.-C., DEMEKHIN, E. A., KOPELEVICH, D. I. & YE, Y. 1997 Nonlinear wavenumber selection in gradient-flow systems. *Phys. Rev. E* **55**, 2818.

CHANG, H.-C., DEMEKHIN, E. A., ROBERTS, R. M. & YE, Y. 1999 Modulation wave dynamics of kinematics interfacial waves. In *Fluid Dynamics at Interfaces* (ed. W. Shyy & R. Narayanan), pp. 99–112. Cambridge University Press.

CHANG, H.-C., DEMEKHIN, E. A. & YE, Y. 1996b Coarsening dynamics of falling-film solitary waves. *Phys. Rev. E* **54**, 1467.

CHARRU, F. & BARTHELET, P. 1999 Secondary instabilities of interfacial waves due to coupling with a long wave mode in a two-layer Couette flow. *Physiaca* D **125**, 311.

CHENG, M. & CHANG, H.-C. 1995 Competition between subharmonic and sideband secondary instabilities of a falling film. *Phys. Fluids* **7**, 34.

CHU, K. J. & DUKLER, A. E. 1974 Statistical characteristics of thin wavy films. *AIChE J.* **20**, 695.

FRISCH, U., SHE, Z. S. & THUAL, O. 1986 Viscoelastic behaviour of cellular solutions to the Kuramoto-Sivashinsky model. *J. Fluid Mech.* **168**, 221.

KRANTZ, W. B. & GOREN, S. L. 1971 Stability of thin liquid films flowing down a plane. *Ind. Engng Chem.* **10**, 91.

LIU, J. & GOLLUB, J. P. 1994 Solitary wave dynamics on film flows. *Phys. Fluid* **6**, 1702–1711.

RAMASWAMY, B., CHIPPADA, S. & JOO, S. W. 1996 A full-scale study of interfacial instabilities on thin-film flows. *J. Fluid Mech.* **325**, 163.

RUYER-QUIL, CH. & MANNEVILLE, P. 1998 Modeling film flows down an inclined plane. *Eur. Phys. J.* **B6**, 277.

SALAMON, T. R., ARMSTRONG, R. C. & BROWN, R. A. 1994 Traveling waves on inclined films: numerical analysis by the finite-element method. *Phys. Fluids* **6**, 2202.

SANGALLI, M., McCREADY, M. J. & CHANG, H.-C. 1997 Stabilization mechanism of short waves in stratified gas-liquid flow. *Phys. Fluids* **9**, 919.

SHKADOV, V. YA. 1967 Wave conditions in the flow of thin liquid layer of a viscous liquid under the action of gravity. *Izu. Akad. Nauk SSSR, Mekh. Zhidk. Gaza* **1**, 43.

STAINTHORP, F. P. & ALLEN, J. M. 1965 The development of ripples on the surface of a liquid film flowing inside a vertical tube. *Trans. Inst. Chem. Engrs* **43**, 85.

VLACHOGIANNIS, M. & BONTOZOGLOU, V. 2001 Observations of solitary wave dynamics of film flows. *J. Fluid Mech.* **435**, 191.